Momentum transport from tearing modes with shear flow[a)]

F. Ebrahimi,[b)] V. V. Mirnov, and S. C. Prager
Department of Physics and Center for Magnetic-Self Organization in Laboratory and Astrophysical Plasmas, University of Wisconsin-Madison, Madison, Wisconsin 53706, USA

A theoretical and computational study of momentum transport from reconnection from tearing modes in the presence of sheared flow in a reversed field pinch has been performed. Momentum transport from single tearing modes in the linear and nonlinear regimes and transport from multiple tearing modes is studied. It is found that, whereas a single mode produces transport, a strong enhancement in transport arises from the nonlinear coupling of multiple modes. A single tearing mode, in the presence of equilibrium flow, produces momentum transport in the vicinity of the reconnection layer. This is demonstrated from quasilinear calculation of Maxwell and Reynolds stresses. However, nonlinear, resistive magnetohydrodynamics computation of the full, multimode nonlinear dynamics reveals an additional effect. In the presence of multiple tearing modes, nonlinear coupling strongly enhances the torques and broadens their radial width. The resulting transport from current-driven instability is much more rapid than classical viscous forces. © *2008 American Institute of Physics*. [DOI: 10.1063/1.2838247]

I. INTRODUCTION

Toroidal plasmas are often observed to rotate in the toroidal direction, in both astrophysical and laboratory settings. It is also observed in both venues that the toroidal angular momentum can be rapidly transported in the radial direction. For example, in accretion disks surrounding black holes, as particles fall radially in toward the black hole, angular momentum is transported radially outward. That is, such transport is needed to maintain a Keplerian rotation profile as individual particles gain momentum from inward motion. In the toroidal laboratory configuration of the reversed field pinch (RFP), rapid momentum transport occurs as a flattening of the radial profile of the toroidal rotation during a reconnection event, and momentum transport is also inferred from edge measurements.[1,2] In both cases, momentum transport is faster than can be explained by collisional viscosity. Also, for both cases the leading explanations of momentum transport are stresses (Maxwell and Reynolds) arising from magnetohydrodynamic (MHD) instabilities: A flow-driven instability for accretion disks (e.g., Refs. 3 and 4) and a current-driven instability for the RFP.[5]

In this paper, we theoretically examine the laboratory example of momentum transport from current-driven reconnection, a process possibly also relevant to astrophysical plasmas. In the RFP, the dominant instabilities are resistive tearing modes, nonlinearly coupled to each other. Coupling between three tearing modes with different wave numbers can produce localized torques that alter the radial distribution of the toroidal and poloidal momenta, thereby transporting momentum. This notion was introduced previously through analysis of the ideal MHD equations away from the resonant surfaces.[6,7]

The physics of momentum transport is investigated through both quasilinear calculations and full nonlinear MHD computations of torques. First we examine torques arising from a single tearing mode in the linear regime with the flow velocity of order $V_0 \approx S^{-1/5} V_A$. We display the analytic solutions for the Maxwell and Reynolds stresses from quasilinear theory and from computational solution of the exact linearized equations. While linear theory cannot predict the magnitude of the stresses, it provides the spatial structure, which proves to be very similar to that in the nonlinear regime. Using both quasilinear theory and linear computation, we find that single tearing mode transports momentum. Single tearing mode produces nonzero Maxwell and Reynolds torques in the presence of mean shear flow. The torques are localized to the reconnection layer. We then compute the stresses for the full nonlinear evolution of a single tearing mode. For the low viscosity selected for the nonlinear, single mode computation, the Reynolds stress dominates and yields a momentum transport rate 1000 times faster than that due to classical viscosity. Finally, we compute the complete case of multiple, nonlinearly coupled tearing modes. Comparison to the single nonlinear mode reveals the important additional effects that arise from nonlinear coupling. The torques are strengthened. The effect of multiple tearing modes is not merely the superposition of independent, radially separated effects. Rather, the torque arising from the stress of one spatial mode (among many) is itself increased by the presence of other modes. For example the phase between the current density and magnetic field of a specific mode is altered (from the case of one mode only) so as to increase the Maxwell stress.

Some features of the theoretical predictions presented here are consistent with the experimental measurements. The increase in correlation of the phase (between the current density and magnetic field) in the multiple tearing mode computations is consistent with the experimental measurement of the phase during a sawtooth crash in the Madison Symmetric

---

experiment (MST). Preliminary MST measurements also show that both Maxwell and Reynolds stresses are strong during the sawtooth crash when nonlinear mode coupling is important.[8] Moreover, in the edge region of the Extrap-T2R, experimental measurement of Maxwell and Reynolds stresses suggests a strong relation between the $m=0$ tearing mode activity and the momentum transport at the edge.[2] However, a more complete comparison between the theoretical prediction of momentum transport from tearing modes and RFP experiments awaits further experimental measurements of stresses in the whole plasma during the sawtooth cycle.

The nonlinear, 3D, resistive MHD code DEBS[9] is employed to study momentum transport from tearing modes in both linear and nonlinear states at zero pressure,

$$\frac{\partial \bar{A}}{\partial t} = S\bar{V} \times \bar{B} - \eta \bar{J}, \tag{1}$$

$$\rho \frac{\partial \bar{V}}{\partial t} = -S\rho \bar{V} \cdot \nabla \bar{V} + S\bar{J} \times \bar{B} + \nu \nabla^2 \bar{V} + \mathbf{F}(r), \tag{2}$$

$$\bar{B} = \nabla \times \bar{A}, \tag{3}$$

$$\bar{J} = \nabla \times \bar{B}, \tag{4}$$

where $S = \tau_R/\tau_A$ (Lundquist number), $\nu = \tau_R/\tau_{vis}$ (magnetic Prandtl number = viscosity/resistivity), and time is normalized to the diffusion time. An axial *ad hoc* momentum source term $\mathbf{F}(r)$ is added to the momentum equation to generate mean flow. The linear single mode computations are performed with specified flow profile which is fixed in time. The flow velocity used in the linear computations are $V_0 = 0.001 - 0.4 V_A$. The nonlinear evolution of a single tearing mode and full multiple tearing mode computations are performed with a uniform *ad hoc* source. The nonlinear multiple mode computations are at Lundquist number up to $S = 5 \times 10^4$ with axial flow velocities $V_z = 0.03 - 0.07 V_A$, very similar to MST flow velocities.

The paper is organized as follows: In Sec. II, momentum transport from a single tearing mode is investigated. The quasilinear calculation of Maxwell and Reynolds stresses in both reconnection layer (inner layer) and outer (ideal) regions are presented in Sec. II A. The results of single mode computations in the linear regime are discussed in Sec. II B. We also discuss nonlinear evolution of single mode in Sec. II B. We present full nonlinear multiple tearing mode computations in Sec. III, and we then summarize in Sec. IV.

II. SINGLE TEARING MODE

We investigate momentum transport from a single tearing mode. Quasilinear torques are calculated through both analytical calculations and single tearing mode computations in the presence of shear flow. In Sec. II A, we first obtain the inner layer equations in the presence of shear flow ($V_0 \approx S^{-1/5} V_A$) in the cylindrical geometry and then calculate quasilinear Maxwell and Reynolds stress terms in the inner and outer regions. We also perform single tearing mode com-

putations in the linear regime and compare the stress terms with quasilinear calculations in Sec. II B. In the absence of shear flow the stresses are zero in both the outer and inner layer regions. We find that in the presence of shear flow, the main contribution of momentum transport arises from the inner layer solutions. The outer ideal solutions produce nonzero but very small stresses. We also present the result of linear stability analysis of tearing mode with shear flow, and find the destabilizing effect in the small shear flow regime and stabilization of the tearing mode at higher shear. The flattening of the flow profile during the nonlinear evolution of a single mode will be also discussed.

A. Quasilinear calculations

We first calculate the quasilinear torque arising from a single tearing mode. Linear tearing modes with equilibrium flows,[10–12] and the effect of shear flow on resistive tearing instability in slab geometry[13–16,22] have been studied previously. Here, we concentrate on the torque and employ a cylindrical plasma with equilibrium helical magnetic field (azimuthal and axial fields) and axial flow. The assumed flow, $V_z(r)$, is weak, and therefore is only negligibly destabilizing due to its shear dV_z/dr.[14,16] We solve for the eigenfunctions in the resistive, reconnection layer (which is smaller than the island width) and in the ideal, outer regions, from which we construct the Lorentz force ($\tilde{J} \times \tilde{B}$, where tilde denotes perturbations) arising from the Maxwell stress and the fluid force arising from the Reynolds stress ($\rho \tilde{\mathbf{V}} \cdot \nabla \tilde{\mathbf{V}}$). Consider a force-free equilibrium with perturbations of the form $\tilde{a}(r, \theta, z, t) = \tilde{a}(r) \exp(\gamma t + im\theta - ik_z z)$, the linearized resistive MHD equations with flow are,

$$\rho \gamma^2 \xi + \rho \gamma (\mathbf{V}_0 \cdot \nabla) \xi + \rho \gamma (\xi \cdot \nabla) \mathbf{V}_0$$
$$= (\nabla \times \tilde{\mathbf{B}}) \times \mathbf{B} + \mathbf{J} \times \tilde{\mathbf{B}} - \nabla \tilde{p},$$

$$\tilde{p} + 1/\gamma (\mathbf{V}_0 \cdot \nabla)\tilde{p} = -(\xi \cdot \nabla p) - \Gamma p \nabla \cdot \xi, \tag{5}$$

$$\tilde{\mathbf{B}} - \eta/\gamma \nabla^2 \tilde{\mathbf{B}} = \nabla \times (\xi \times \mathbf{B}) + 1/\gamma \nabla \times (\mathbf{V}_0 \times \tilde{\mathbf{B}}).$$

We adopt tearing ordering[23] $\gamma \propto \eta^{3/5}$, $\gamma \to \epsilon^3$, $\eta \to \epsilon^5$, $(r - r_s) \to \epsilon^2 x$, where r_s denotes the resonant surface ($k_\parallel = 0$) and ϵ is a small parameter. We assume $g = \mathbf{k} \cdot \mathbf{V}_0 = -k_z V_z$ vanishes at the resonant surface ($r = r_s$) and varies linearly with x in the inner region, $g = g'(r_s)x$, where $g'(r_s)$ determines the shear flow in the inner region. We consider a small equilibrium flow of order $V_0 \approx \eta^{1/5}$ $[g = (k \cdot V_0)'_{(r_s)}x \to \epsilon^3]$. The rest of the parameters in Eq. (5) are as in Ref. 23. We expand the displacement and magnetic field perturbations in powers of ϵ: $\xi = \epsilon^2(\xi_r^{(2)} + \cdots)\mathbf{e}_r + (\xi_b^{(0)} + \cdots)\mathbf{B} + (\xi_\perp^{(0)} + \cdots) \times \mathbf{e}_r \times \mathbf{B}$, $\tilde{\mathbf{B}} = \epsilon^4(\tilde{B}_r^{(4)} + \epsilon^2 \tilde{B}_r^{(6)} + \cdots)\mathbf{e}_r + \epsilon^4(\tilde{B}_b^{(4)} + \cdots)\mathbf{B} + \epsilon^4(\tilde{B}_\perp^{(4)} + \cdots)\mathbf{e}_r \times \mathbf{B}$. The radial and parallel components of the induction equation become

$$\tilde{B}_r^{(4)} - \frac{\eta}{\gamma}\tilde{B}_r^{(6)''} = (\mathbf{B} \cdot \nabla)\xi_r^{(2)} - \frac{ig}{\gamma}\tilde{B}_r^{(4)}, \tag{6}$$

$$-\frac{\eta}{\gamma}\widetilde{B}_b^{(4)\prime\prime} = -(\nabla\cdot\xi)^{(2)} + (\mathbf{B}\cdot\nabla)\xi_b^{(0)} - \frac{(p+B^2)^\prime}{B^2}\xi_r^{(2)}$$

$$+\frac{1}{\gamma}\frac{(B_zV_z^\prime)}{B^2}\widetilde{B}_r^{(4)}. \tag{7}$$

The parallel, perpendicular, and the annihilated [using the operator $\nabla\cdot(\mathbf{B}\times/B^2)$] components of the momentum equation are

$$\rho\gamma^2\left(1+\frac{ig}{\gamma}\right)\xi_b^{(0)} + \rho\gamma\frac{(B_zV_z^\prime)}{B^2}\xi_r^{(2)} = \frac{-p^\prime\widetilde{B}_r^{(4)} - (\mathbf{B}\cdot\nabla)\widetilde{p}^{(4)}}{B^2}, \tag{8}$$

$$-iB^2(k_\perp B)\widetilde{B}_b^{(4)} = (J\cdot B)\widetilde{B}_r^{(4)} + i(k_\perp B)\widetilde{p}^{(4)}, \tag{9}$$

$$\rho\gamma^2\left(1+\frac{ig}{\gamma}\right)\xi_r^{(2)\prime\prime} = (\mathbf{B}\cdot\nabla)\widetilde{B}_r^{(6)\prime\prime} + i(k_\perp B)\frac{(J\cdot B)^\prime}{B^2}\widetilde{B}_r^{(4)}$$

$$+\frac{2B_\theta^2}{rB^2}(k_\perp B)^2\widetilde{B}_b^{(4)}, \tag{10}$$

where equilibrium quantities are defined at the resonant surface, $k_\perp B|_{r_s} = mB^2/r_sB_z$ and $\mathbf{B}\cdot\nabla|_{(r\to r_s)} = -(imB_zq^\prime/q^2R)x$, where $q = rB_z/RB_\theta$. Combining Eqs. (6)–(10) without pressure gradient terms, the inner layer equations for the radial magnetic field, displacement and parallel magnetic field, with the effect of flow shear are

$$\Psi_2^{\prime\prime} = \Omega\left[X\Xi + \left(1+i\frac{G^\prime X}{\Omega}\right)\Psi_0\right], \tag{11}$$

$$\left(1+i\frac{G^\prime X}{\Omega}\right)\Xi^{\prime\prime} = \frac{X^2\Xi}{\Omega} + \left[\frac{X}{\Omega}\left(1+i\frac{G^\prime X}{\Omega}\right) - \frac{J_p}{\Omega^2}\right]\Psi_0$$

$$-\frac{\Upsilon}{\Omega^2}, \tag{12}$$

$$\Upsilon^{\prime\prime} = \left(\frac{X^2}{\Omega\left(1+i\dfrac{G^\prime X}{\Omega}\right)} + \frac{2\Omega\left(1+i\dfrac{G^\prime X}{\Omega}\right)l^6}{\Gamma\beta}\right)\Upsilon$$

$$+\Omega\left(S_q + \frac{iG^\prime G_p X}{\left(1+i\dfrac{G^\prime X}{\Omega}\right)}\right)\Xi + \left(-\frac{JX^2}{\Omega\left(1+i\dfrac{G^\prime X}{\Omega}\right)}\right.$$

$$\left.-\frac{2\Omega\left(1+i\dfrac{G^\prime X}{\Omega}\right)Jl^6}{\Gamma\beta} + iG^\prime G_p\right)\Psi_0, \tag{13}$$

where dimensionless length and frequency scales are X and

Ω. An inverse time scale Ω_R and a resistive length scale $L_R = (\eta/\Omega_R)^{1/2}$ are considered and the following dimensionless quantities are used:

$$F^\prime = -\frac{q^\prime B_\theta}{qB},$$

$$S_q = \left(\frac{2a}{Rq^\prime}\right)^2, \quad \beta = \frac{2p}{B^2}; \quad B = |B(r_s)|,$$

$$\Omega_R = \left(\frac{m^2\eta F^{\prime 2}B^2}{\rho r_s^2}\right)^{1/3}, \quad l = (L_R/r_s)^{1/5},$$

$$\Omega = \gamma/(l^4\Omega_R), \quad X = x/(lL_R),$$

$$J = \frac{2B_\theta^2}{F^\prime BB_z}\left(\frac{J\cdot B}{B^2}\right), \quad J_p = \frac{r_s}{F^\prime BB_z}(J\cdot B)^\prime,$$

$$\Xi = \xi_r^{(2)}, \quad \Upsilon = -\frac{2r_sa^2B^2}{l^6R^2B_\theta^2q^{\prime 2}}\widetilde{B}_b^{(4)},$$

$$\Psi_0 = \frac{ir_s}{L_RmF^\prime Bl}\widetilde{B}_r^{(4)}, \quad \Psi_2 = \frac{ir_s}{L_RmF^\prime Bl^7}\widetilde{B}_r^{(6)},$$

$$G_p = -\frac{2\rho^{1/2}a^2B_z\Omega_R}{l^5k_zR^2B_\theta^2q^{\prime 2}}, \quad G^\prime = (\eta r_s^3/\Omega_R^6)^{1/5}g^\prime.$$

The equations reduce to those of a slab[14–16] when the curvature term [last term of Eq. (12)] is zero. With change of variable $h = \Omega(\Xi + iG^\prime\Psi_0/\Omega)$, and $\mu = \sqrt{2}x$, radial magnetic field perturbation and the displacement become

$$(\Omega + i\lambda_G\mu)h^{\prime\prime} - \frac{\mu^2}{4}h = -\frac{\Upsilon}{2} + \Omega\mu - \lambda_F, \tag{14}$$

$$\Psi_2^{\prime\prime} = \frac{\mu}{4}h + \Omega,$$

where $\lambda_F = \sqrt{2}J_p$, $\lambda_G = G^\prime/\sqrt{2}$. Without curvature term, these equations are similar to the equations in slab geometry with the growth rate given in Ref. 14. The growth rate increases with flow shear as λ_G^2 in the limit of small flow shear.

In the absence of mean flow ($G^\prime, G_p = 0$), Eqs. (12) and (13) are solved using the expansion of Ξ and Υ in terms of Hermite polynomials,

$$\Xi = \exp(-Z^2/2)\Sigma_n a_n H_n(Z),$$

$$\Upsilon = \exp(-Z^2/2)\Sigma_n b_n H_n(Z), \tag{15}$$

where $Z = \Omega^{-1/4}X$. We keep the even parts of the solutions (the terms containing J and J_p). The even parts of the solutions which they do not enter the growth rate calculations and usually are ignored,[23] are important for the stress term calculations. The odd and even part of the coefficients are obtained,

$$a_{2m+1} = \frac{2^{1/2}\Psi_0}{\Omega^{1/4}4^m m!}\left[\frac{\left(4m+3+\frac{2l^6\Omega^{3/2}}{\Gamma\beta}\right)}{-(4m+3)\left(4m+3+\frac{2l^6\Omega^{3/2}}{\Gamma\beta}\right)-S_q}\right],$$

$$a_{2m} = \frac{-2^{1/2}\Psi_0}{4^m m!}$$
$$\times\left[\frac{\frac{J_p}{\Omega^{3/2}}\left(4m+1+\frac{2l^6\Omega^{3/2}}{\Gamma\beta}\right)+\frac{2Jl^6}{\Gamma\beta}+\frac{J(4m+1)}{\Omega^{3/2}}}{-(4m+1)\left(4m+1+\frac{2l^6\Omega^{3/2}}{\Gamma\beta}\right)-S_q}\right],$$

$$b_{2m+1} = \frac{-2^{1/2}\Psi_0}{\Omega^{-5/4}4^m m!}\left[\frac{S_q}{-(4m+3)\left(4m+3+\frac{2l^6\Omega^{3/2}}{\Gamma\beta}\right)-S_q}\right],$$

$$b_{2m} = \frac{2^{1/2}\Psi_0}{4^m m!}\left[\frac{S_q J_p - (4m+1)\left(\frac{2Jl^6\Omega^{3/2}}{\Gamma\beta}+J(4m+1)\right)}{-(4m+1)\left(4m+1+\frac{2l^6\Omega^{3/2}}{\Gamma\beta}\right)-S_q}\right]. \tag{16}$$

We use the flow shear ordering for the parallel magnetic field and displacement,

$$\xi_r^{(2)} = \xi_{r0}^{(2)} + iG'\xi_{rG}^{(2)} - G'^2\xi_{rG}^{(2)} + \cdots,$$
$$\tilde{B}_b^{(4)} = \tilde{B}_{b0}^{(4)} + iG'\tilde{B}_{bG}^{(4)} - G'^2\tilde{B}_{bG}^{(4)} + \cdots, \tag{17}$$

where $\xi_{rG}^{(2)}$ and $\tilde{B}_{bG}^{(4)}$ are the first order solutions with flow shear. From this expansion, we obtain first order solutions at the low resistivity limit in terms of the zeroth order solutions (solutions without flow shear, expressible as a sum of Hermite functions),

$$Y_{\text{odd}}^{(1)} \approx \left[-\frac{(S_q+G_p)Z\Xi_{\text{even}}^{(0)}}{\Omega^{-3/4}}\right]\bigg/\left(Z^2+\frac{S_q}{Z^2}\right),$$

$$Y_{\text{even}}^{(1)} \approx \left[-\frac{(S_q+G_p)Z\Xi_{\text{odd}}^{(0)}}{\Omega^{-3/4}}+\frac{(S_q-G_p)\Psi_0}{\Omega^{-1/2}}\right]\bigg/\left(Z^2+\frac{S_q}{Z^2}\right), \tag{18}$$

and we construct the axial Maxwell stress term $[\langle\tilde{J}\times\tilde{B}\rangle_z = (1/r)\langle r\tilde{B}_r\tilde{B}_z\rangle']$, where $\langle\rangle$ denotes flux surface averaged]. The part of the force that is even about $r=r_s$ is related to the current gradient at the resonant surface. The nonzero contribution of the inner layer quasilinear Lorentz term can be obtained, $\langle\tilde{J}\times\tilde{B}\rangle_b = 1/4r\,d/dr(r\tilde{B}_r\tilde{B}_b^*) = -2G'(\Psi_0 L_R mF'l^7R^2B_\theta^2 q'^2/2r_s^2 a^2B)dY^{(1)}/dr$. The Lorentz force is directly proportional to the flow shear (G') in the limit of small flow shear. Even part of the Lorentz force is
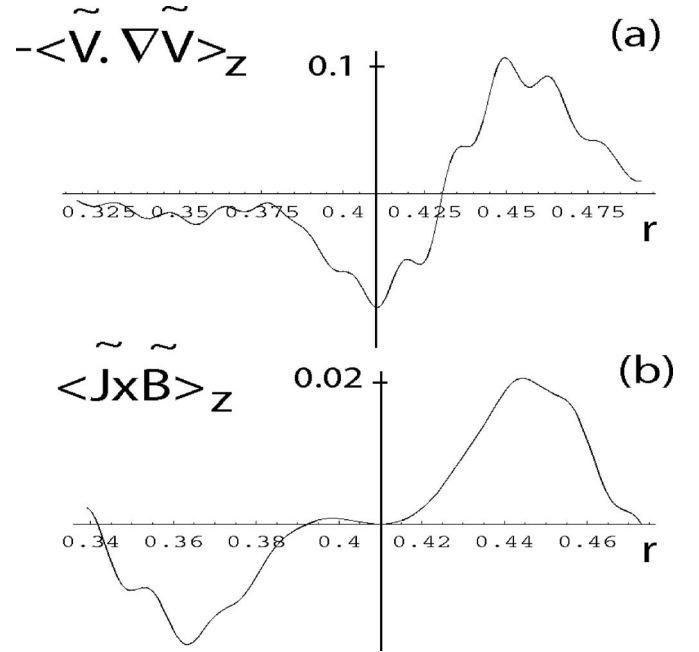

FIG. 1. The analytical quasilinear inner layer solutions for (a) the axial fluid stress, $-\langle\tilde{V}\cdot\nabla\tilde{V}\rangle_z$, and (b) the axial Lorentz force, $\langle\tilde{J}\times\tilde{B}\rangle_z$. The origin is the location of the resonant surface. The solutions are for the core tearing mode, $m=1$ and $k_z=2.0$. The small oscillations are an artifact of the Hermite series truncation.

related to the even part of the radial displacement, and therefore to the current gradient at the resonant surface. Note that the Lorentz force without flow vanishes due to a 90° phase shift between $\tilde{B}_{b0}^{(4)}$ and $\tilde{B}_r^{(4)}$.

Using the parallel displacement,

$$\xi_b^{(0)} = \frac{1}{\rho\gamma(\gamma+ig'x)}$$
$$\times\left\{-\rho\gamma\xi_r^{(2)}\frac{(B_zV_z')}{B^2}+\frac{(\mathbf{B}\cdot\nabla)}{B^2}\left[B^2\tilde{B}_b^{(4)}+\frac{(\mathbf{J}\cdot\mathbf{B})}{i(k_\perp B)}\tilde{B}_r^{(4)}\right]\right\}, \tag{19}$$

we construct the Reynolds stress, $[\langle\tilde{V}\cdot\nabla\tilde{V}\rangle_b = (\gamma^2/r) \times\langle r\xi_r^{(2)}\xi_b^{(0)}\rangle']$, using an expansion similar to Eq. (17). Expressing the first order solutions in terms of shear flow, the Lorentz force and the Reynolds stress are calculated for the inner layer region are shown in Fig. 1. The solutions are for the core tearing mode, $m=1$ and $k_z=2.0$ with an equilibrium current $\lambda = J_\parallel/B = \lambda_0(1-r^\alpha)$ ($\lambda_0=3.2$ and $\alpha=3$, $S=10^4$, $\Delta'=6.1$). The solutions are localized around resonant surface and radially integrate to zero. Thus, these structures transport momentum to reduce the flow gradient while conserving the total momentum in the plasma. The radial width is determined by the resistive layer width, unrelated to the width of the resulting magnetic island.

We also obtain the stress terms from a single tearing mode in the outer (ideal) region. The incompressible ideal
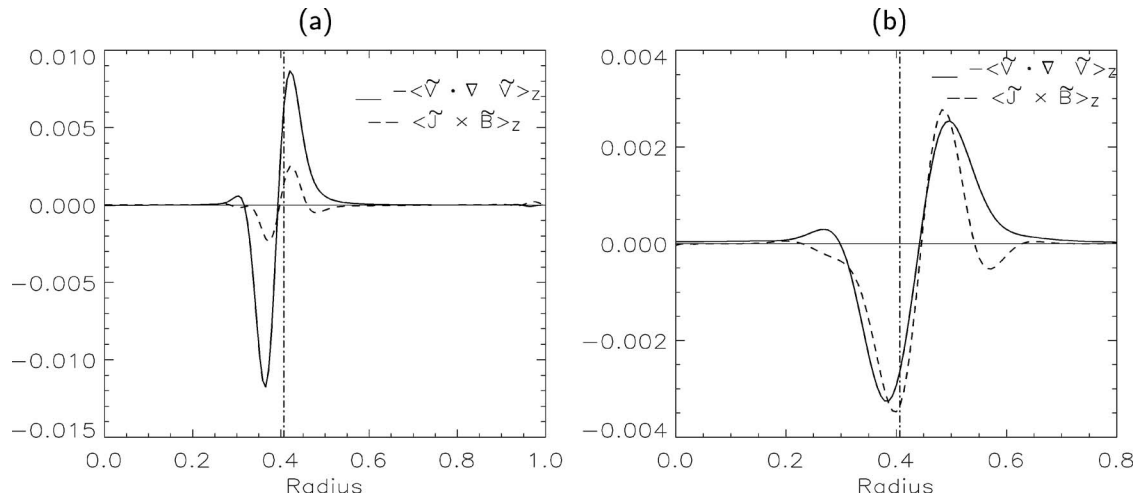
FIG. 2. Axial fluid stress $-\langle \tilde{V} \cdot \nabla \tilde{V} \rangle_z$ and axial Lorentz force $\langle \tilde{J} \times \tilde{B} \rangle_z$ from linear single mode computations ($\rho = 1$); (a) $P_m = 0.01$, (b) $P_m = 1.0$.

MHD equations are linearized in the presence of mean shear flow. We assume perturbation of the form $Q(r, \theta, z, t) = Q(r)\exp[i\omega t + i(m\theta - k_z z)]$, and the equilibrium magnetic field and flow are $\mathbf{B} = B_\theta(r)\mathbf{e}_\theta + B_z(r)\mathbf{e}_z$ and $\mathbf{V}_0 = V_z(r)\mathbf{e}_z$, respectively. The linearized equations can be combined and be presented in the form of one ordinary differential equation for $\tilde{V}_r$,

$$(r\tilde{V}_r)'' + c1(r\tilde{V}_r)' + c2(r\tilde{V}_r) = 0, \tag{20}$$

where

$$c1 = \frac{1}{A}\frac{dA}{dr} + \frac{k_z V_z'}{\Omega_o},$$

$$c2 = \frac{1}{A}\left\{ -\frac{d}{dr}\left(\frac{k_z V_z' A}{\Omega_o}\right) - \frac{2k^2 B_\theta V_z' k_\perp B}{\Omega_o^2(m^2 + k_z^2 r^2)} - \frac{d}{dr}\left[\frac{2m B_\theta F}{r\Omega_o(m^2 + k_z^2 r^2)}\right] \right.$$
$$\left. + \frac{2B_\theta}{r\Omega_o}\left(\frac{B_\theta}{r}\right)' + \frac{4k_z^2 B_\theta^2}{r\Omega_o(1 - M^2)(m^2 + k_z^2 r^2)} - \frac{F^2(1 - M^2)}{r\Omega_o} + \frac{2B_\theta^2 k_z V_z'}{r^2 \Omega_o^2} \right\}, \tag{21}$$

$$A = \frac{rF^2(1 - M^2)}{\Omega_o(m^2 + k_z^2 r^2)}, \quad \Omega_o = \omega - k_z V_z, \quad M = \sqrt{\rho}\frac{\Omega_o}{F}, \quad F = \frac{m B_\theta}{r} - k_z B_z, \quad k_\perp B = m B_z/r + k_z B_\theta,$$

where $\omega = \omega_r + i\gamma$, and $\omega_r = k_z V_z|_{(r = r_s)}$ leading to finite $M = \sqrt{\rho}\Omega_o/F$ at the rational surface (with $\gamma = 0$). The equation for parallel magnetic field perturbations in terms of radial velocity perturbation is obtained,

$$\tilde{\mathbf{B}} \cdot \mathbf{B} = iA\left\{\frac{\partial}{\partial r}(r\tilde{V}_r) - \left[\frac{2m B_\theta}{(1 - M^2)Fr^2} - \frac{k_z V_z'}{\Omega_o}\right](r\tilde{V}_r)\right\}. \tag{22}$$

We note that parallel magnetic field perturbation is purely imaginary when ω is real (with zero growth rate) and is out of phase with the radial magnetic field. Axial Lorentz force is calculated using Eq. (22), $\tilde{B}_r = F\tilde{V}_r/\Omega_o$ and

$\tilde{B}_z = m\tilde{B}_\parallel / rk_\perp - iB_\theta/(Brk_\perp)\partial/\partial r(r\tilde{B}_r)$. The Lorentz term from a single tearing mode in the outer region is

$$\langle \tilde{J} \times \tilde{B} \rangle_z = \frac{\gamma}{r}\left[\rho\frac{V_z(r_s) - V_z(r)}{k_\perp F^2}km|\tilde{B}_\parallel^{(0)}|\tilde{B}_r\right]'$$
$$+ \frac{2\gamma}{r}\left[\rho\frac{V_z(r_s) - V_z(r)}{k_\perp(m^2 + k_z^2 r^2)F^2 B}km^2 B_\theta \tilde{B}_r^2\right]', \tag{23}$$

where γ is the growth rate, and $\tilde{B}_\parallel^{(0)} = i[Fr(r\tilde{B}_r)' - r(k_\perp B)\lambda(r\tilde{B}_r)]/[B(m^2 + k_z^2 r^2)]$ is the parallel field without mean flow from the Newcomb[25] equation, and $\lambda = J_\parallel/B$. In the absence of mean flow, it can be seen from the solutions
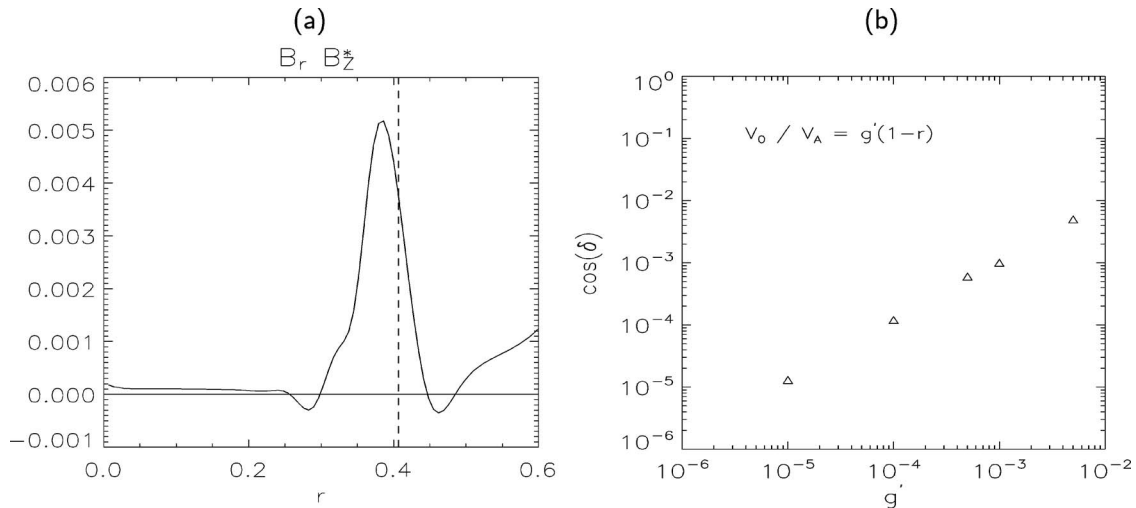
FIG. 3. (a) Radial structure of $\cos(\delta)$, where δ is the phase between $\widetilde{B}_r$ and $\widetilde{B}_z^*$ with $P_m=0.01$ $(\langle \widetilde{J} \times \widetilde{B} \rangle = 1/r[r|\widetilde{B}_z||\widetilde{B}_r|\cos(\delta)]')$. The vertical line denotes the location of the resonant surface. (b) $\cos(\delta)$ vs small mean flow shear, g' for mean flow of $V_0/V_A = g'(1-r)$.

of Newcomb equation, that $\widetilde{B}_r$ and $\widetilde{B}_\parallel^{(0)}$ are out of phase, and parallel and axial Lorentz forces vanish for the ideal region. With mean flow shear, Eq. (7) shows that the joint effect of mode growth and flow shear produces nonzero torque. Since

the tearing growth rate scales as $S^{-3/5}$, where S is the Lundquist number, the single mode Lorentz term is small in the outer region. Axial fluid Reynolds term is similarly calculated,

$$\langle \widetilde{V} \cdot \nabla \widetilde{V} \rangle_z = \frac{2\gamma}{r}\left(\rho \frac{(V_z(r_s) - V_z(r)^3 k_z^4 m B_\theta}{(m^2 + k_z^2 r^2)F\{F^2 - \rho k_z^2[V_z(r_s) - V_z(r)]^2\}^2} r \widetilde{B}_r^2\right)'. \tag{24}$$

It is seen that the fluid stress term is also proportional to the growth rate, and is small in the outer region. Therefore, the

major contribution of single tearing mode to momentum transport arises from the inner layer solutions.
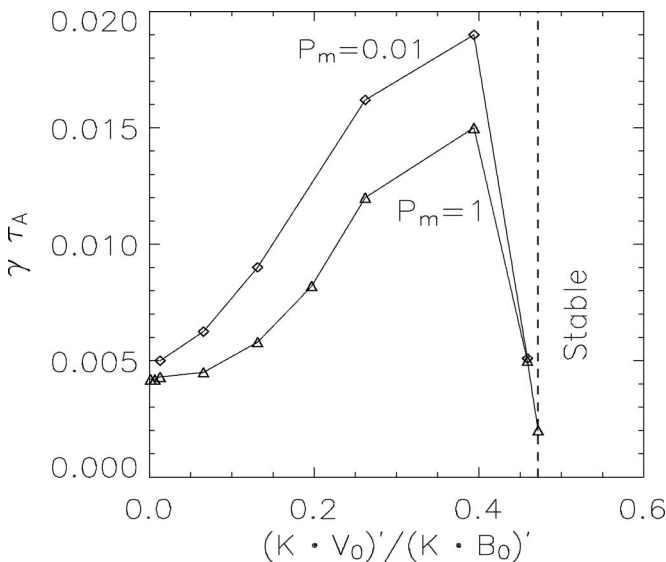
FIG. 4. Core tearing mode growth rate vs the ratio of shear flow to the magnetic shear ($S=10^4$) for two Prandtl numbers. $\diamond$ and $\triangle$ denote $P_m=0.01$ and $P_m=1$, respectively.
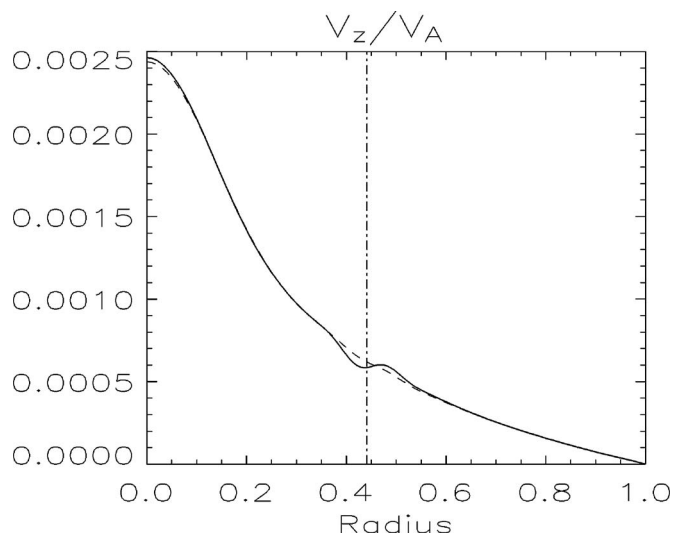
FIG. 5. Radial profile of axial flow (averaged over axial and azimuthal directions) for a single mode in its initial state (dashed line) and nonlinear state (solid line).
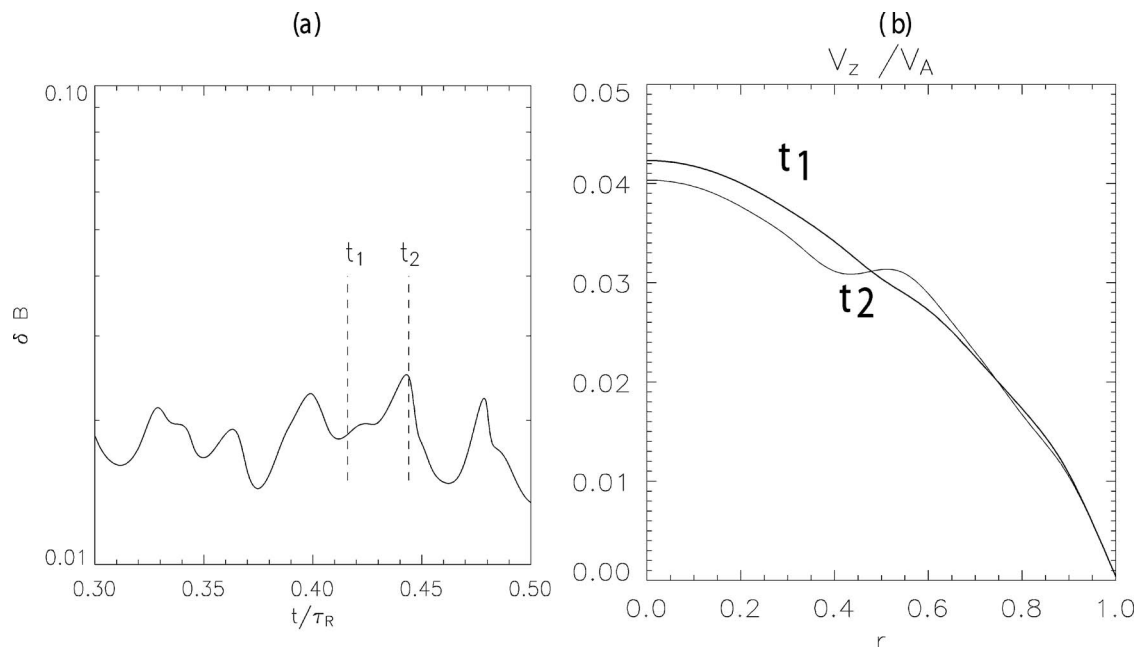
FIG. 6. (a) Total magnetic fluctuation $\sqrt{1/2\int B_r^2 dv}$ vs time ($S=10^4$). (b) Flow profile for times t_1 and t_2.

B. Linear and nonlinear single mode computations

Momentum transport from a single tearing mode is studied using MHD computations in the linear and nonlinear regime. The computations are performed using the DEBS code. It is shown that the approximate analytic quasilinear results found in Sec. II A are consistent with computational solution of the full MHD equations in the linear regime. For the linear computations, the flow profile is specified and fixed in time. We choose the equilibrium magnetic field and flow profiles which are identical to those of the analytical calculations in the previous section. Also equivalent to the analytic calculations, the computations are performed in the nonviscous regime, $P_m < 0.4 S^{-2/5} \Delta'^{6/5} F'^{-2/5} \rho^{1/5}$,[24] with $P_m = \nu/\eta = 0.01$, where ν and P_m are viscosity and the magnetic Prandtl number, respectively. Figure 2 shows the fluid stress term, $\langle \widetilde{V} \cdot \nabla \widetilde{V} \rangle_z$, and Lorentz term, $\langle \widetilde{J} \times \widetilde{B} \rangle_z$, for two

regimes, resistive, nonviscous ($P_m=0.01$), and viscoresistive ($P_m=1.0$), during the linear growth phase. The stresses in the nonviscous regime are localized and similar in radial structures to the analytic solutions. There are some differences in detail, likely arising from the constant ψ approximation of the analytics, which is not true for the computation. In the nonviscous regime, both the computation and quasilinear calculations yield a fluid stress term five times larger than the Maxwell stress [Figs. 1 and 2(a)]. The two stresses are comparable at higher viscosity [Fig. 2(b)].

The nonzero contribution of $\langle \widetilde{J} \times \widetilde{B} \rangle_z$, arises from the phase between $\widetilde{B}_r$ and $\widetilde{B}_z$ around the resonant surface [Fig. 3(a)]. This phase increases linearly with the flow shear in agreement with the quasilinear calculations discussed in Sec. II A. Figure 3(b) shows that the linear phase increases with
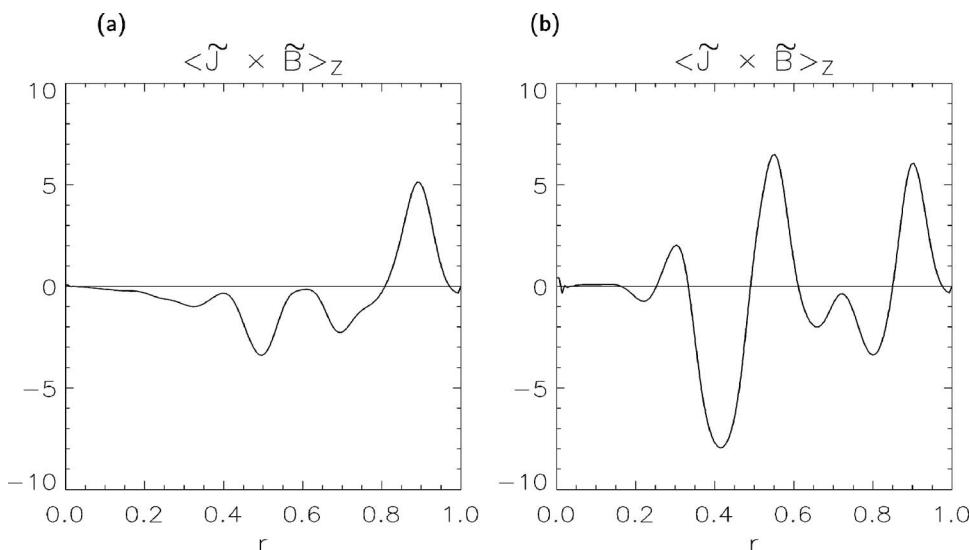

FIG. 7. Radial structures of (a) total $\langle \widetilde{J} \times \widetilde{B} \rangle_z$ term at $t_1=0.416$ and (b) at $t_2=0.444$ (summed over all n and m mode numbers) ($S=10^4$).
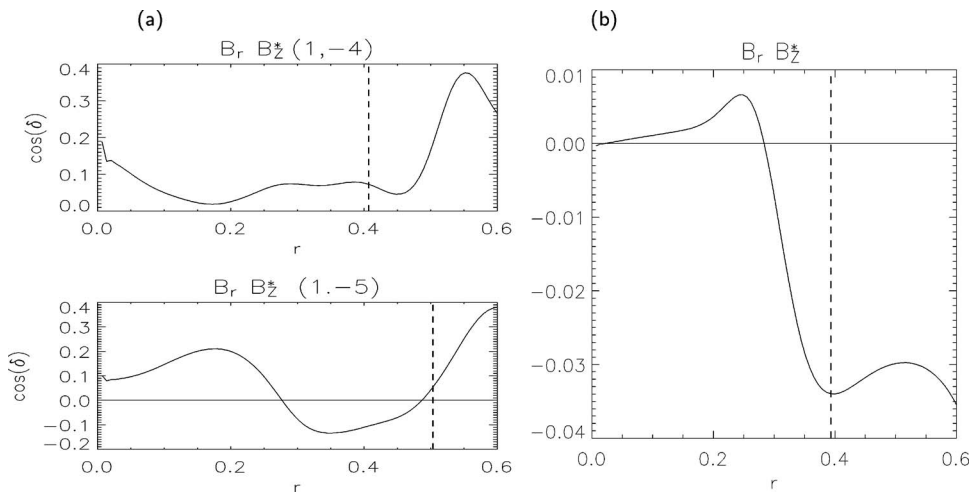
FIG. 8. Radial structure of $\cos(\delta)$, where δ is the phase between $\widetilde{B}_r$ and $\widetilde{B}_z^*$. (a) Nonlinear phase from multiple mode computations; (b) single mode phase from single mode computation.

small mean flow shear. For zero shear flow, $\widetilde{B}_r$ and $\widetilde{B}_z$ are 90° out-of-phase and therefore corresponds to zero Lorentz force.

The effect of parallel shear flow on the resistive tearing instability has been studied in slab geometry.[13–15,19] Using constant $-\psi$ approximations, the growth rate modification of the tearing modes with sub-Alfvénic shear flow was found.[14,15] The growth rate of tearing instability was shown to increase by the small shear flow and the scaling with S remained unchanged ($S^{-3/5}$). However, later a more general treatment of shear flow effects was considered using the nonconstant-ψ tearing modes.[16] A stabilizing effect was found, when the flow shear is larger than the magnetic field shear. The effect of viscosity on the tearing growth rate with shear flow was also studied.[15,17,18,20] It was found that the growth rate scaling alters as $S^{-2/3}P_m^{-1/6}$. Here, we perform linear computation of a core tearing mode with force free equilibrium [with equilibrium current $J_\parallel/B=3.2(1-r^3)$] with shear flow in the cylindrical geometry. The result of linear MHD computations of a core tearing mode, $m=1$, $k_z=2.0$, with mean shear flow at $S=10^4$, and with $P_m=0.01$ and $P_m=1$ is shown in Fig. 4. The equilibrium magnetic field is fixed (and thus the magnetic shear) and only the shear flow is changed. As is seen the tearing mode growth rate is increased for small shear flow and the tearing mode becomes stable at larger shear flow. The results are consistent with the linear theory[14–17] in slab geometry. When the ratio of shear flow to magnetic shear is very small {for $[(k\cdot V_0)']/(k\cdot B_0)')<0.13$ or $V_0/V_A<0.05$} the growth rate does not change. For larger values of the ratio of shear flow to magnetic shear [0.13 $<(k\cdot V_0)']/(k\cdot B_0)')<0.47$ or $0.05<V_0/V_A<0.3$ growth rate increases. At higher shear flow, the tearing mode becomes stable for both Prandtl numbers. At higher shear, the tearing mode can transition to Kelvin–Helmholtz instability.[21]

To examine the nonlinear evolution of a single mode (as well as the multimode case), we again employ the DEBS code, but with an *ad hoc* momentum source $F(r)$ added to the momentum equation. The source is added to generate flow. The transport is then determined by plasma fluctuations. The effect of the forces on the flow during the nonlinear phase of a single mode computation with $P_m=0.01$ is

shown in Fig. 5. The flow profile is flattened around the resonant surface, as for the analytical calculations. The flow flattens very rapidly, in about one thousandth of a viscous diffusion time (or 0.05 resistive diffusion times). Separate computation in which the flow is chosen to be dominantly perpendicular or dominantly parallel (to the equilibrium field) reveal that both flows are flattened similarly.

III. MULTIPLE TEARING MODE COMPUTATIONS

Here, we investigate full nonlinear dynamics of momentum transport in the RFP using multiple tearing mode computations. Computation with multiple tearing modes, as occurs in the RFP, reveals the additional effects of nonlinear
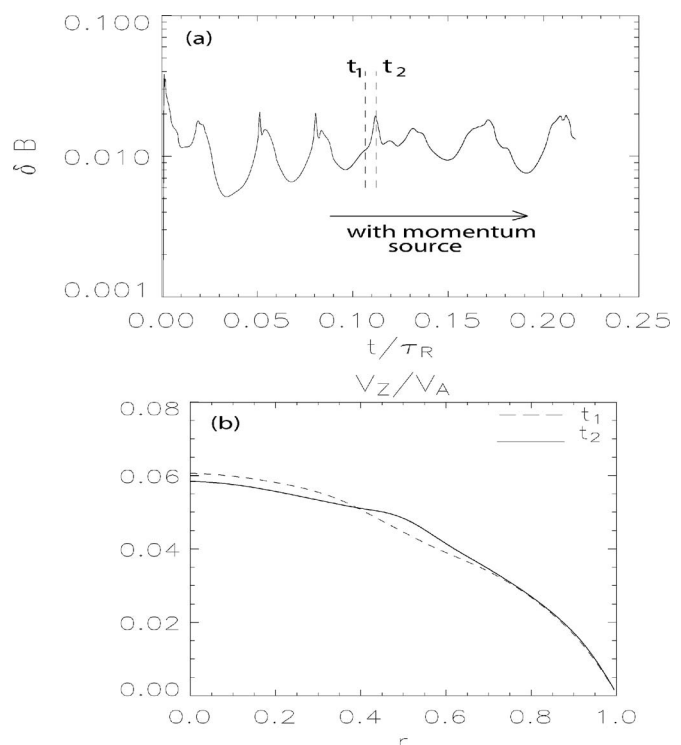

FIG. 9. (a) Total volume integrated magnetic fluctuations $\sqrt{1/2\int B_r^2 dv}$ vs time. (b) Plasma flow profiles for times t_1 and t_2 ($S=5\times10^4$).

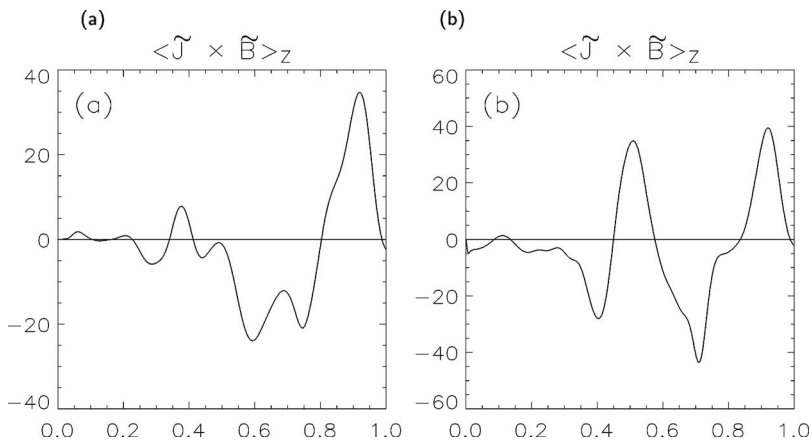FIG. 10. Radial structures of (a) total $\langle \tilde{J} \times \tilde{B} \rangle_z$ term at $t_1/\tau_R = 0.11$ and (b) at $t_2/\tau_R = 0.112$ (summed over all n and m mode numbers).

mode coupling. The role of magnetic reconnection and nonlinear mode coupling on momentum transport is studied with an *ad hoc* momentum source added to the axisymmetric momentum equation (in DEBS code). The simulations are started with standard nonlinear RFP simulation, $F(r)=0$ (with $P_m = 10$, aspect ratio $R/a = 1.66$ and radial, azimuthal, and axial resolutions $n_r = 200$, $n_\theta = 16$ and $n_z = 128$, respectively). After reaching a quasistationary RFP state, $F(r)$ is switched on with a profile $F(r) = $ const. The radial structure of the force is such that the axial flow profile would become parabolic in radius in the absence of fluctuation-induced stresses. Computations with $S = 10^4$ and $S = 5 \times 10^4$ are presented.

Total magnetic fluctuations for the computation with $S = 10^4$ is shown in Fig. 6. The *ad hoc* source is applied at $t/\tau_R = 0.3$ and axial flow velocity reaches a value of $V_z \approx 0.04 V_A$. Flow profiles for two times ($t_1/\tau_R = 0.416$ and $t_2/\tau_R = 0.444$) are shown in Fig. 6(b). When the fluctuations are low during a sawtooth oscillation (at $t_1/\tau_R = 0.416$), the Lorentz force is small as shown in Fig. 7 and the flow profile remains close to the parabolic flow profile. Total Lorentz force is strong when fluctuations are high (at $t_2/\tau_R = 0.444$) and changes sign around $r = 0.4 - 0.6$ which result in fattening of the flow profile [Fig. 6(b)]. In the multiple mode computations, the Reynolds stress is small, since the flow fluctuations are reduced by viscosity. The individual nonlinear Lorentz forces are large and the nonlinear phase (between B_r and

B_z) becomes stronger than a single tearing mode phase (Fig. 8). The phase of a single tearing mode with $V_z = 0.045 V_A$ is shown in Fig. 8(b). The nonlinear phases for $m=1$, $n=-4$ and $m=1$, $n=-5$ modes from the multiple tearing computation is a few times larger than the single tearing mode phase, showing nonlinear coupling enhances the Lorentz forces and thus the momentum transport.

We also perform computations at higher Lundquist number $S = 5 \times 10^4$. In these computations more pronounced sawtooth events are observed. $F(r)$ is switched on at $t/\tau_R = 0.085$ with a profile $F(r) = $ const. The tearing fluctuations undergo a repetitive sawtooth cycle, as shown in Fig. 9(a). After the force is applied the axial flow builds, saturating at $V_z = 0.06 V_A$ [Fig. 9(b)]. However, the flow is strongly influenced by the sawtooth oscillations of the fluctuations. The flow profiles for two times, t_1 and t_2, are shown in Fig. 9(b). As is seen, the flow becomes flatter in the core at time t_2 when fluctuations are large. The flattening arises from the Lorentz force from tearing fluctuations, shown in Fig. 10(b) for time t_2. The Lorentz force at time t_1 is small in the core [Fig. 10(a)] and causes a peaked flow profile. The Lorentz terms for $m=1$ and $m=0$ modes at time t_2 are also shown in Fig. 11(a). It is seen that the main contribution of the total Lorentz term arises from the $m=1$ modes. The Lorentz force arises from multiple tearing modes, as shown in Fig. 11(b)
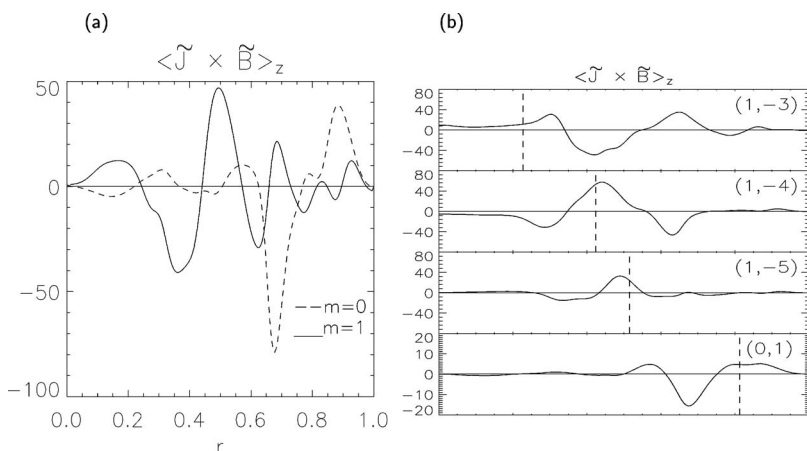

FIG. 11. Radial structure of (a) total $\langle \tilde{J} \times \tilde{B} \rangle_z$ force for $m=1$ and $m=0$ modes (summed over all n numbers), (b) $\langle \tilde{J} \times \tilde{B} \rangle_z$ force for a subset of individual modes [with $(m,n)=(1,-3)$, $(1,-4)$, $(1,-5)$, $(0,1)$] for time $t_2/\tau_R = 0.112$.
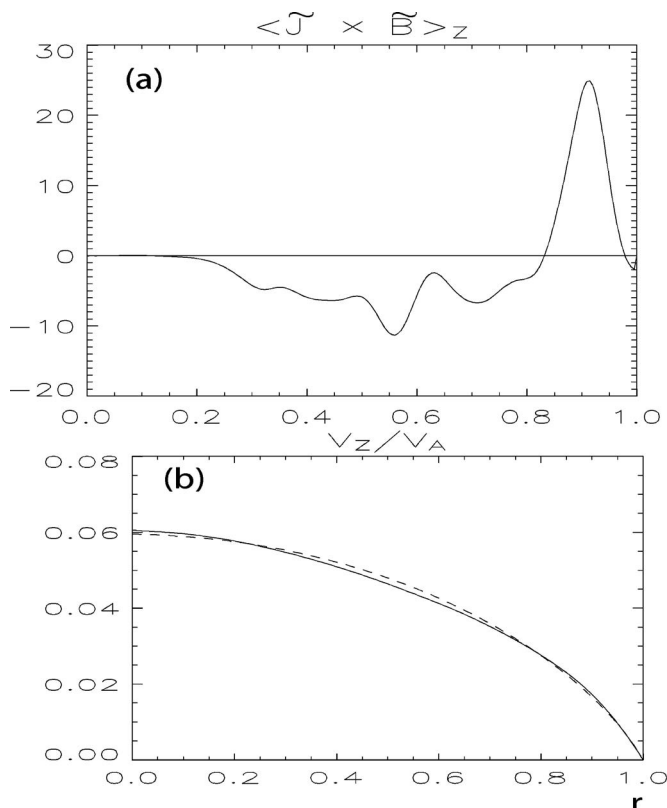
FIG. 12. (a) Total Lorentz $\langle \tilde{J} \times \tilde{B} \rangle_z$ force without $m=0$ modes. (b) Flow profiles without total fluctuations (dashed line) and without $m=0$ modes (solid line).

for several $m=1$ modes ($n=-3$ to $n=-5$) resonant in the core and $m=0$ mode resonant near the edge.

The observed momentum transport is much more rapid than would occur without fluctuations. The time scale for flattening is about one-tenth of the viscous diffusion time scale. Moreover, this comparison understates the effect of the tearing stresses. To isolate the effect of the tearing modes, we have performed a computation in which the modes are turned off at t_1, immediately before the onset of the momentum-flattening reconnection event. We observe that the flow profile *peaks* due to the modest dominance of the *ad hoc* force over viscous diffusion. Thus, the flattening dominantly occurs from the tearing stresses. The exception is the edge, where the torques localized at about $r/a \approx 0.92$ (Fig. 10) is countered by viscous torques arising near the no-slip boundary. Although the Lorentz force from each mode is largest around its resonant surface, the radial width is substantially larger than that of a single mode. Apparently, nonlinear coupling broadens the radial structures.

To clarify the effect of nonlinear coupling, we perform nonlinear computation in which the $m=0$ mode is removed. It is known that the $m=0$ mode mediates the coupling between $m=1$ modes (with different n values). As a result, computation without $m=0$ modes eliminates the dominant $m=1$ mode coupling. The plasma evolves to a quasisteady state without sawtooth oscillations. The Lorentz force is reduced about fourfold across 80% of the plasma radius, as shown in Fig. 12(a). The structure of the force is also altered, now being unidirectional in the core. Thus, the flattening of

the flow profile does not occur [Fig. 12(b)], and momentum transport is greatly reduced.

IV. SUMMARY

In summary, through quasilinear theory and nonlinear MHD computations, we have established that the Maxwell and Reynolds stresses arising from tearing instabilities can transport momentum rapidly in the RFP. We have calculated the Maxwell and Reynolds stresses from a single tearing mode both in the outer (ideal) region and the reconnection layer. We find that the major contribution to momentum transport from a single tearing mode arises from the inner-layer solutions in the presence of mean shear flow. We have also performed linear stability analysis of tearing modes with shear flow in cylindrical geometry, and find a destabilizing effect in the small shear-flow regime and stabilization at higher shear. Through nonlinear MHD computations, we show that the a single tearing mode can transport momentum much more rapidly than classical viscous forces. Moreover, the inclusion of multiple tearing modes, resonant at different radii, substantially increases momentum transport. Nonlinear mode coupling amplifies the transport. The nonlinear coupling between $m=1$ modes in the presence of the $m=0$ mode causes momentum transport. The Lorentz force, and therefore momentum transport, is greatly reduced in the computations without $m=0$ modes. By eliminating the $m=0$ mode, the three wave coupling is greatly reduced. Aspects of the theoretical results are consistent with experiment[1] (such as the effect of nonlinear coupling on the phase shift between current and magnetic field fluctuations in the Maxwell stress). However, much of the theoretical predictions awaits experimental test. We are investigating whether current-driven reconnection can transport momentum in astrophysical situations. In future work, we will report the comparison between momentum transport from the flow-driven magnetorotational instabilities, and from the current-driven reconnection in disk geometry.

[1] A. K. Hansen, A. F. Almagri, D. Craig, D. J. Den Hartog, C. C. Hegna, S. C. Prager, and J. S. Sarff, Phys. Rev. Lett. **85**, 3408 (2000).
[2] N. Vianello, V. Antoni, E. Spada, M. Spolaore, G. Serianni, R. Cavazzana, H. Bergsaker, M. Cecconello, and J. R. Drake, Nucl. Fusion **45**, 761 (2005).
[3] S. A. Balbus and J. F. Hawley, Astrophys. J. **376**, 214 (1991).
[4] B. Coppi and P. S. Coppi, Phys. Rev. Lett. **87**, 051101 (2001).
[5] F. Ebrahimi, V. V. Mirnov, S. C. Prager, and C. R. Sovinec, Phys. Rev. Lett. **99**, 075003 (2007).
[6] C. C. Hegna, Phys. Plasmas **3**, 4646 (1996).
[7] R. Fitzpatrick, Phys. Plasmas **6**, 1168 (1999).
[8] G. Fiksel, A. F. Almagri, J. K. Anderson, T. M. Biewer, A. P. Blair, D. L. Brower, B. E. Chapman, D. Craig, D. J. Den Hartog, W. X. Ding, C. B. Forest, C. C. Hegna, R. Gatto, J. Goetz, K. J. McCollam, V. V. Mirnov, R. O'Connell, S. C. Prager, J. C. Reardon, J. S. Sarff, P. W. Terry, and S. D. Terry, in Proceedings of 19th IAEA Fusion Energy Conference, Paper EX/P4-01 (2002). Available at http://www.iaea.org/programmes/ripc/physics/fec2002/html/node247.htm#55127.
[9] D. D. Schnack, D. C. Barnes, Z. Mikic, D. S. Harned, and E. J. Caramana, J. Comput. Phys. **70**, 330 (1987).
[10] D. Dobrott, S. C. Prager, and J. B. Taylor, Phys. Fluids **20**, 1850 (1977).
[11] R. K. Pollard and J. B. Taylor, Phys. Fluids **22**, 126 (1979).
[12] R. Gatto, P. W. Terry, and C. C. Hegna, Nucl. Fusion **42**, 496 (2002).
[13] I. Hofmann, Plasma Phys. **17**, 143 (1975).
[14] R. B. Paris and W. N-C. Sy, Phys. Fluids **26**, 2966 (1983).

[15]A. Bondeson and M. Persson, Phys. Fluids **29**, 2997 (1986).
[16]X. L. Chen and P. J. Morrison, Phys. Fluids B **2**, 495 (1990).
[17]X. L. Chen and P. J. Morrison, Phys. Fluids B **2**, 2575 (1990).
[18]R. B. Paris, A. D. Wood, and S. Stewart, Phys. Fluids B **5**, 1027 (1993).
[19]G. Einaudi and F. Rubini, Phys. Fluids **29**, 2563 (1986).
[20]G. Einaudi and F. Rubini, Phys. Fluids B **1**, 2224 (1989).

[21]L. Ofman, X. L. Chen, P. J. Morrison, and R. S. Steinolfson, Phys. Fluids B **3**, 1364 (1991).
[22]J. M. Finn, Phys. Plasmas **2**, 4400 (1995).
[23]B. Coppi, J. M. Greene, and J. L. Johnson, Nucl. Fusion **6**, 101 (1966).
[24]A. Bondeson and J. R. Sobel, Phys. Fluids **27**, 2028 (1984).
[25]W. A. Newcomb, Phys. Fluids **10**, 232 (1960).